Front. Environ. Sci. Eng. 2022, 16(3): 27
https://doi.org/10.1007/s11783-021-1461-z

RESEARCH ARTICLE

Valorization of agro-industrial fruit peel waste to fluorescent nanocarbon sensor: Ultrasensitive detection of potentially hazardous tropane alkaloid

Athiyanam Venkatesan Ramya (✉), Manoj Balachandran

Nanocarbon Research Group, Materials Science Research Laboratory, Department of Physics and Electronics, CHRIST (Deemed to be University), Bengaluru- 560029, Karnataka, India

HIGHLIGHTS

- Transformation of agro-industrial waste to value-added material via green chemistry.
- Orange peel is valorized into fluorescent nanodiamond-like carbon (fNDC) sensor.
- fNDC detects potentially hazardous drug atropine sulfate (AS).
- fNDC recognizes AS in biological fluids and pharmaceuticals.
- fNDC assures applications in clinical and forensic toxicology.

GRAPHIC ABSTRACT

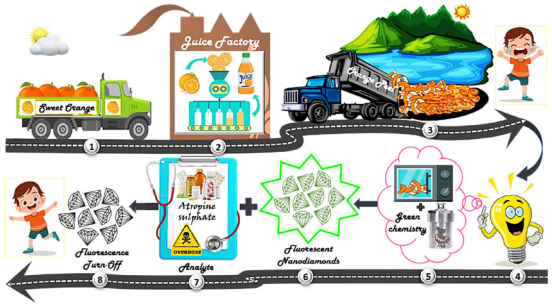

ARTICLE INFO

Article history:
Received 9 December 2020
Revised 29 April 2021
Accepted 11 May 2021
Available online 8 June 2021

Keywords:
Agro-industrial waste
Orange peel
Valorization
Nanodiamond-like carbon
Atropine sulphate
Fluorescence sensing

ABSTRACT

Millions of tonnes of agro-industrial waste are generated each year globally, with the vast majority of it going untreated, underutilized, and disposed of by burning or landfilling, causing severe environmental distress and economic downturn. A practical solution to this global issue is to use green chemistry to convert this waste into value-added products. Accordingly, in the present study, agro-industrial orange peel waste was valorized into fluorescent nanodiamond-like carbon sensor via a green route involving hydrothermal treatment of microwave carbonized orange peel waste. The developed sensor, used for the fluorescence detection of potentially hazardous drug atropine sulfate, exhibits unique dual linearity over concentration ranges of 300 nM to 1 M and from 1 M to 10 M, as well as ultra-low sensitivity of 34.42 nM and 356.46 nM, respectively. Additionally, the sensor demonstrates excellent reproducibility, high stability, and satisfactory recovery when used to identify and quantify atropine sulfate in biological samples and commercially available pharmaceuticals, indicating promising multidisciplinary applications.

1 Introduction

With an annual global production of around 45 million tonnes, orange is one of the top five fruits that dominate global fruit markets. On average, approximately 23 million tonnes of sweet oranges are processed for juice production. Since the edible part of this citrus fruit is relatively small, a large portion of nearly 13 million tonnes of solid waste is generated each year, with the peel being the principal constituent. (Wikandari et al., 2015). This agro-industrial waste is either burned or dumped in the land adjacent to the orchard or landfills, resulting in uncontrolled greenhouse-gas production and a threat to the local watercourses. Fresh peel is difficult to dispose of safely due to its inherent high acidity and low protein content, as it is rarely used as livestock feed or in conventional waste treatment methods (Meneguzzo et al., 2019). Ergo, considering the magnitude of this global issue, it is high time to valorize this waste into value-added products.

In recent years, an intense upsurge of interest in the

✉ Corresponding author
E-mail: avramyaa1@gmail.com

research and development of nanodiamonds (NDs) is observed, owing to its nano size, optical transparency from UV to IR spectral regions, low/negative electron affinity, wide band gap, and stable fluorescence, which all contribute to their unique optical and electrical properties (Nunn et al., 2017). In 1963, Russian scientists developed a detonation technique for the production of diamond nanocrystals by exploding an oxygen-deficient (2-methyl-1,3,5-trinitrobenzene)/ RDX (1,3,5-trinitroperhydro-1,3,5-triazine) mixture in a closed chamber (Mandal et al., 2014). Since then, several other techniques for producing NDs have been reported, including laser ablation of graphite, high-energy ball milling of microcrystalline diamond synthesized by High-Pressure and High-Temperature (HPHT) method, Microwave Plasma Chemical Vapor Deposition (MWCVD), hydrothermal treatment of certain chlorinated hydrocarbons, microplasma dissociation of ethanol vapor, ultrasonic cavitation of graphite and low-grade coal at ambient conditions, etc. (Xiao et al., 2015b).

The invention of luminescent NDs in 2005 revolutionized the domain of fluorescent carbon materials, opening exciting new horizons of NDs research. Experiments with fluorescent nanodiamonds (fNDs) in recent years have exemplified their diverse applications, especially in materials science and medicine, including quantum information processing, bioimaging, nanosensing, and drug delivery (Stursa et al., 2016). However, when compared to other fluorophores that are readily synthesized via wet chemistry, the production of fNDs is quite challenging. NDs are bombarded with high-energy atomic/subatomic particles in order to displace the carbon atoms so as to create internal defects in the ND lattice. This results in the formation of optically active centers termed vacancy centers, of which Nitrogen-Vacancy (N-V), Silicon Vacancy (Si-V), Europium (Eu-V), and Boron Vacancy (B-V) are popular (Hsiao et al., 2016).

Fluorescent sensors are a boon to analytical sensing due to their high sensitivity, selectivity, rapid response rate, and technical simplicity. Of the various types of available fluorescent probes, organic dyes are popular. Although most of the fluorescent organic dyes exhibit good quantum yields, a lot of them undergo photobleaching upon continuous excitation (Kumar et al., 2018). Quantum Dots (QDs) have large Stokes shifts, high fluorescence quantum yields, and non-quenching fluorescence; however, they are toxic and hence not biocompatible. Even though upconversion nanoparticles (UCNPs) and gold nanoparticles are biocompatible and photostable, their quantum yield is low, and emission rates are slow. Nevertheless, fNDs may be the best substitutes for these traditional probes in numerous sensing applications owing to their unique attributes like high biocompatibility, tailorable surface chemistry, and exceptional photophysical properties like infinite photostability, absence of photo blinking, and long fluorescence lifetime (>10 ns) (Shenderova et al., 2017). Most commercial fNDs are produced with (N-V) color centers that emit in the red/NIR region. To compete with the rest of the available fluorophores, the production of fNDs with other emission wavelengths is highly significant for various applications in diverse fields.

Alkaloids are well-known for their noxious properties, which can occur as a result of inadvertent or intentional ingestion. Atropine is an important tropane alkaloid extracted from certain Solanaceae plants. Due to its anticholinergic, antispasmodic, and antidote characteristics, atropine has extensive therapeutic applications. Atropine is most commonly used in medicine in its sulfate form ($(C_{17}H_{23}NO_3)2H_2SO_4H_2O$), which is the active pharmaceutical ingredient used to treat parkinsonism, septic shock, myopia, peptic ulcers, diarrhea, bronchial asthma, cardiopathy, and organophosphate poisoning, among other conditions. (Dar et al., 2012). The potency of atropine is crucial in therapeutics because an inadequately low dose of atropine does not yield expected remedial effects, whereas an abnormally high dose is lethal and causes atropism by stimulating the central nervous system. Several cases of overdose have been reported with a ~50% atropism rate and ~18.3% mortality rate. The TDLo (oral minimal toxic dose) of atropine for mankind is 33 μg/kg (Khataee et al., 2018). At times, even the usual clinical dosage might be harmful as the pharmacokinetics and toxic reactions of atropine are related to considerable interpersonal susceptibility (Tom et al., 2016). Apart from its wide clinical applications, the misuse of atropine with criminal intents in suicides and homicides is also reported in the literature (Kerchner and Farkas, 2020). In the light of the foregoing, simple, sensitive, reliable, and rapid recognition and quantification of potentially lethal atropine sulfate (AS) are imperative in drug quality control to ensure proper formulation in the development of this drug.

In this regard, herein, we report the valorization of agro-industrial orange peel waste to value-added fluorescent nanodiamond-like carbon (fNDC) sensor via a facile, economical, scalable, and environmentally benign technique. The fNDC sensor could detect even nanomolar concentrations of AS with wide and dynamic linear range and ultralow detection limits. Additionally, the sensor's ability to detect AS in biological fluids and pharmaceutical formulations has been evaluated. The findings elucidate the feasibility and applicability of the developed fNDC sensor for real-time analysis in clinical pharmacokinetics, pharmaco-toxicology, quality control, and forensics. No previous report, to the best of our knowledge, has established the transformation of agro-industrial orange peel waste to fNDC via green chemistry and the identification and quantification of AS using fNDC derived from agro-industrial orange peel waste via a green route.

2 Experimental

2.1 Materials

The necessary chemicals and solvents of analytical grade were procured and utilized without any purification. Deionized and doubly distilled water was used in all the experiments. Atropine sulfate and scopolamine hydrobromide were purchased from Sigma-Aldrich, India. Atropine sulfate 1 mL ampoules (0.6 mg/mL) and Atropine 1% 5 mL eye drops (10 mg/mL) were bought from Samarth Life Sciences Pvt Ltd and Pharmatak Opthalmics Pvt Ltd respectively.

2.2 Methods

2.2.1 Preparation of fluorescent nanodiamond-like carbon material

Orange (Citrus sinensis) peels were collected in Bangalore, India, from a local fruit processing unit. The peels were cleaned thoroughly with water and then air-dried. They were later carbonized in a domestic microwave oven (900 W). The carbonized peels were powdered in a domestic mixer-grinder (750 W). 2 g of the powdered sample was dispersed in 30 mL of 1:1 volume ratio of ethanol: water and ultrasonicated in an ultrasonic processor (30 kHz) at 60°C for two hours. Following that, the mixture was centrifuged and repeatedly washed with deionized water (10,000 r/min). The cleansed precipitate was dialyzed in a dialysis membrane (12 kDa) for three days. The resulting solution was evaporated in vacuum at 70°C. 1 g of the evaporated dry powder was dispersed in 10 mL of water and treated in a hydrothermal autoclave reactor for 24 h at 150°C. The treated mixture was later evaporated at 70°C in vacuum until a dry powder of fNDC was obtained.

2.2.2 Detection of atropine sulfate

A solution of 25 μg/mL fNDC dispersed in phosphate buffer saline (PBS) of pH 7 was poured into a quartz cell with an optical path length of 1 cm. To this solution, 25 μL of various concentrations of AS (0.1 to 60 μM) were added and mixed thoroughly. At room temperature, the fluorescence intensity of fNDC without and with the addition of AS was recorded at an emission wavelength of 520 nm (on exiting at 440 nm). The sensing experiments were repeated thrice to ensure reproducibility.

2.2.3 Specificity measurements for the detection of atropine sulfate

To investigate the selectivity of fluorescence quenching of fNDC toward AS, solutions of common interference species, namely scopolamine, glucose, ascorbic acid, uric acid, and metal ions solutions (K^+, Na^+, Ca^{2+} , Mg^{2+} , Fe^{3+} and Cu^{2+}) of concentrations 10 μM were prepared in PBS (pH = 7). 100 μL of each interferant was added individually to a fixed volume of 25 μg/mL fNDC and mixed thoroughly. The fluorescence intensity of each fNDC-interferent mixture was recorded at 520 nm after exiting at 440 nm at room temperature. The specificity experiments were repeated thrice to ensure reproducibility.

2.2.4 Detection of atropine sulfate in biological fluids and pharmaceuticals

The detection of AS spiked in human serum, human urine, and pharmaceuticals was examined to determine the feasibility of the proposed fNDC sensor. All experiments complied with applicable laws and guidelines of our parent institution. We obtained informed consent from the healthy volunteer who provided blood and urine samples.

The serum was separated from the blood sample by centrifugation at 5000 r/min for 10 min. Apart from a 100-fold dilution of the serum and urine samples, no further pre-treatment was carried out. Spiked samples were readied by mixing three different concentrations of AS to the diluted blood and urine samples. A fixed volume of 25 μg/mL fNDC was thoroughly mixed to aliquots of these solutions, and the fluorescence emission was recorded at 520 nm (λ_{exc} = 440 nm). To conduct the analysis of pharmaceutical formulations, the contents of 10 ampoules of AS solution were mixed thoroughly, and the volume of 5 eye drop bottles was blended. Each sample was quantitatively diluted to 100 mL in distilled water on an individual basis. 25 μg/mL fNDC was thoroughly mixed to aliquots of these solutions, and the fluorescence emission was recorded at 520 nm (λ_{exc} = 440 nm).

2.3 Instrumentation

Transmission Electron Micrographs were acquired using JEM-2100 (JOEL) High-Resolution Transmission Electron Microscope (HRTEM). Scanning Electron Micrographs were taken using JEOL 6390LA Scanning Electron Microscope. UV/Vis spectrometer (Ocean optics JAZ series) and Shimadzu spectrofluorometer (RF5301PC) were used to obtain absorption and fluorescence spectral measurements. The Fluorolog FL-1057 spectrometer from HORIBA (TCSPC) was used to determine the fluorescence lifetime. Raman spectroscopy at a wavelength of 514.5 nm was obtained using a Horiba LabRAM HR spectrometer. The Fourier Transform Infrared (FTIR) spectrum was acquired using a Thermo Nicolet-Avtar 370 spectrometer. Compositional analysis of the samples was performed using polychromatic Mg K X-rays (hν = 1253.6 eV) on the Omicron ESCA probe X-ray Photoelectron Spectrometer (XPS), and the high-resolution photoelectron spectra were deconvoluted using the XPS Peak 4.1 software. Elemental

Vario's EL111 elemental analyzer was used to conduct the CHNS analysis. Voltammetric studies were executed with a three-electrode configuration in an electrochemical workstation (CH 660E) at a scan rate of 0.5 V/s using fNDC/glassy carbon as the working electrode, saturated calomel as the reference electrode, and a platinum wire as the counter electrode in acetonitrile solution containing 0.1 M tetrabutylammonium hexafluorophosphate ($TBAPF_6$).

3 Results and discussion

3.1 Morphological analysis of the synthesized material

The morphological analysis of the synthesized carbon material using HRTEM, as illustrated in Fig. 1(a-c), reveals the formation of agglomerated polyhedral nanostructures with a morphology similar to that of nanodiamonds (Mochalin et al., 2012). The identified reflections in the SAED patterns of the synthesized nanostructures (Fig. 1(d)) correspond well to the nanodiamond diffraction lines, affirming the formation of nanodiamond-like carbon structures (Kurbatov et al., 2010). The size distribution of the nanodiamond-like carbon structures synthesized is heterogeneous, ranging between 50 nm and 200 nm. The SEM images of the synthesized nanomaterial, shown in Fig. S1, reveal highly agglomerated polyhedrons.

3.2 Optical behavior of the synthesized nanodiamond-like carbon material

The synthesized nanodiamond-like carbon material exhibits strong optical absorption in the UV region (Fig. 2(a)) with a long tail extending into the visible-NIR region. The absorption peak at ~208 nm corresponds to the intrinsic absorbance of nanodiamonds (σ-σ* transition). The peaks at ~278 nm, 309 nm, 329 nm, 356 nm, and 452 nm result from the n-Π* transition of C = O bond of the surface oxygen groups (Hao et al., 2019). The absorption spectrum reveals that the nanodiamond-like carbon material synthesized comprises diverse aromatic acenes and multiple fluorophores. These fluorophores possess their respective HOMO (Highest Occupied Molecular Orbital) and LUMO (Lowest Unoccupied Molecular Orbital) levels, thus possessing different bandgaps.

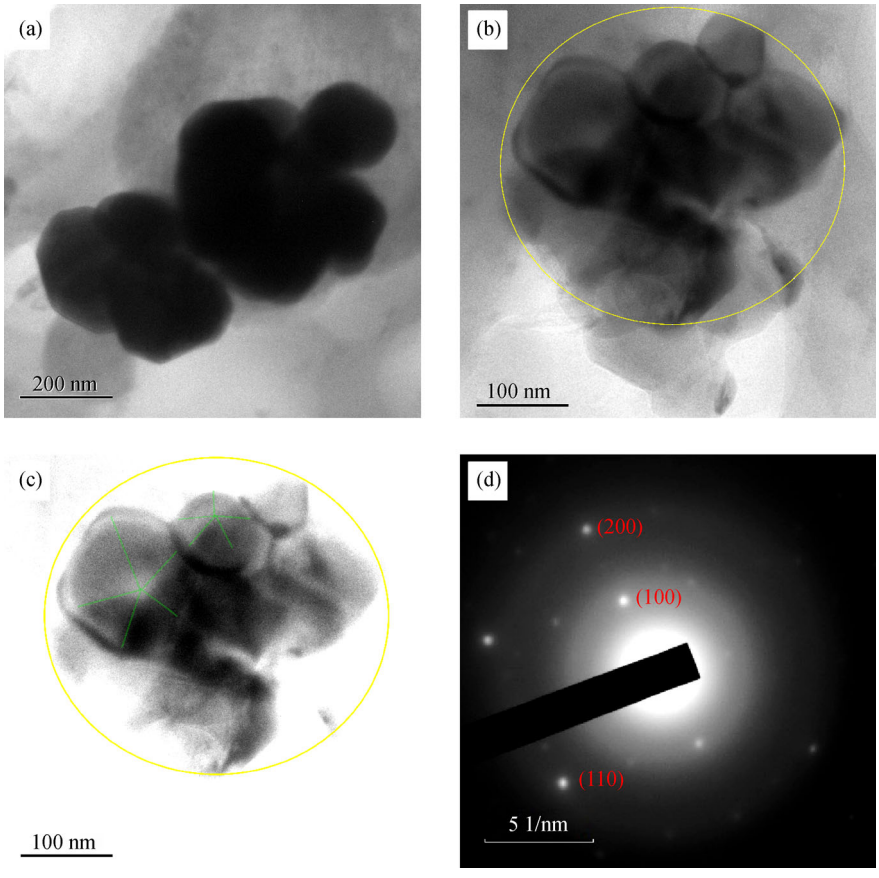

Fig. 1 HRTEM images of carbon nanostructures derived from agro-industrial orange peel waste. (a) HRTEM image exhibiting agglomerated polyhedral nanostructures, (b) Polyhedral structures similar to diamond-like carbon is observed in the encircled portion of the image, (c) An enhanced image of (b) depicting the formation of diamond-like carbon nanostructures, and (d) The selected area diffraction pattern of (b) showing reflections corresponding to nanodiamond phase.

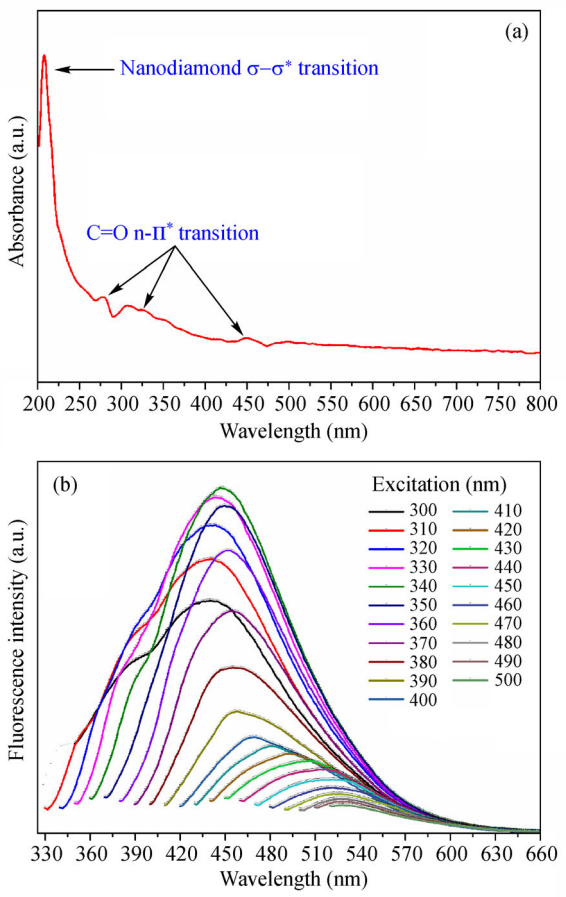

Fig. 2 (a) UV-Visible absorption spectrum of the synthesized nanodiamond-like carbon material, displaying bands corresponding to σ-σ* transition of nanodiamonds and n-Π* transition of C = O functionalities, (b) Steady-state excitation wavelength dependant fluorescence emission spectra of the synthesized fNDC material excited at wavelengths ranging between 300 nm and 500 nm, exhibiting a characteristic red shift.

The fluorescence spectrum of the synthesized nanodiamond-like carbon material (fNDC), for excitation wavelengths (λ_{ex}) between 300 nm and 500 nm, measured at room temperature is portrayed in Fig. 2(b). The fluorescence emission of fNDC increases with increasing excitation wavelength between 300 and 340 nm, with a maximum emission peak observed at ~447 nm (λ_{em}) under 340 nm (λ_{ex}) excitation; the fluorescence emission then decreases with increasing excitation wavelength with a bathochromic shift in the emission peak. In other words, fNDC exhibits excitation wavelength-dependent emission behavior. This phenomenon accounts for the different colors emitted via fluorescence for different excitation wavelengths (Sun et al., 2013).

For a given fluorophore, Stokes shift can be defined as the difference in the positions of the band maxima of the excitation and emission spectra. If the size distribution of the fluorophore affects the fluorescence mechanism, its Stokes shift tends to zero in a linear fashion as the excitation wavelength increases (Xiao et al., 2015a). However, a deviation from this criterion (Fig. S2) suggests that the fluorescence behavior of the synthesized fNDC is governed by a mechanism other than size-induced effects. Due to the high fluorescence of fNDC over a broad range of excitation wavelengths, one possible fluorescence mechanism, (i−e) the interband transition between electrons in the valence and conduction bands, can be ruled out owing to the variance between the band gap of fNDC (refer Fig. S3) and the emissive photon energy (Zhang et al., 2016). Two other prime sources of fluorescence in nanodiamonds include optical/vacancy centers (N-V, Si-V, Eu-V, B-V, etc.) and surface states (Jariwala et al., 2020). In the present case, while it is evident that the synthesized fNDC do not contain any induced vacancy centers, consequently, it is rational to conclude that the fluorescence of fNDC possibly arises from the surface states. Therefore, we hypothesize that the surface functional groups are responsible for the origin of fluorescence in fNDC.

Each functional moiety in fNDC possesses its optimum excitation and emission wavelengths. On varying the excitation wavelength, the corresponding emission wavelength shifts suitably, resulting in excitation-dependent fluorescence. This behavior is attributed to the different types of electronic transitions between the bonding and anti-bonding molecular orbitals of the carbon backbone and the functional groups (Lai et al., 2020). The strongest emission (λ_{em} = 447 nm) exhibits a bright blue hue when excited by a UV band (λ_{ex} = 340 nm), suggesting that OH groups dominate the surface of fNDC (Xiao et al., 2015a). The red-shifted emission of fNDC could be correlated with the relative intensity changes of the different oxygenous groups. It is apparent that the fluorescence of this fNDC can be engineered by tuning the degree of functionalization.

To further evaluate the optical performance of fNDC, the fluorescence quantum yield of fNDC was measured and determined to be 34.03% using quinine sulfate as standard (see Fig. S4 for details). The time-resolved fluorescence decay profile of fNDC was recorded by a time-correlated single-photon counting technique (TCSPC). The decay curve was fitted with a triple-exponential function (Fig. S5), indicating that the fluorescence decay occurs via three relaxation pathways, one due to the intrinsic state and the other two due to surface states. The average fluorescence lifetime of fNDC was calculated to be 8.43 ns (refer Table S1). This relatively long fluorescence is in comparison to the previously reported values (Bray et al., 2015).

The photostability of fNDC material plays an imperative role in its quality and applications in fluorescence detection. In association with this, the fluorescence emission profile of fNDC was examined after exposure to illumination for 6 h. It is discerned from the curve between the fluorescence emission intensity and time that there is minimal observable photo-bleaching witnessed on

irradiation up to 6 h (displayed in Fig. S6), authenticating the excellent photostability of the synthesized fNDC. The high fluorescence quantum yield, the long fluorescence lifetime, and the remarkable photostability of fNDC make it a promising material for multidisciplinary applications.

3.3 Structure and composition of the synthesized fNDC material

The X-ray diffraction pattern of the synthesized fNDC structures is shown in Fig. S7. The strongest observed peak, at $2\theta \sim 43.7°$ corresponds to reflection from (111) nanodiamond planes. The peak at noticed at $2\theta \sim 76.2°$ is attributed to (220) diffraction of nanodiamonds. The peak at $2\theta \sim 25.3°$ is ascribed to the presence of graphitic carbon in the sample (Tang et al., 2016). The formation of nanodiamond-like carbon is confirmed by XRD spectral analysis.

Raman spectroscopy of NDs is not just limited to the identification of the diamond phase but also provides valuable insights into the structure, composition, and information on the surface functionalities. The Raman spectrum of the synthesized fNDC is presented in Fig. 3. Raman spectrum was deconvoluted into individual peaks to elucidate the existence of various functional groups in the sample.

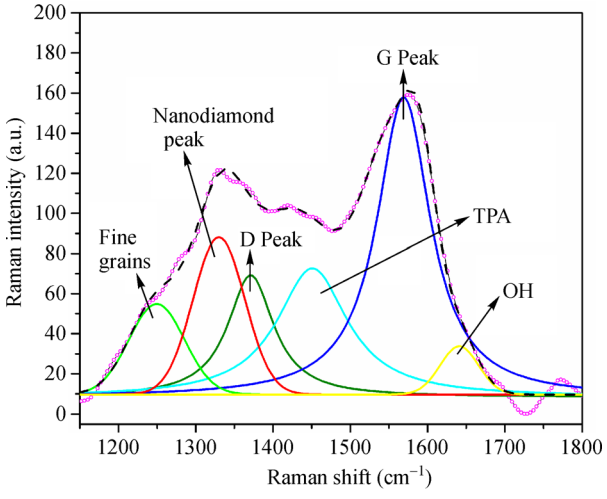

Fig. 3 First-Order Raman spectrum of the synthesized fNDC deconvoluted with peaks corresponding to different moieties. The line interconnected by tiny circles represents the original experimental spectrum, and the colored solid lines represent the deconvoluted peaks. The dotted line represents the sum of the deconvoluted peaks.

The spectral features of fNDC exhibit a typical Raman profile of NDs, with a relevant band positioned at 1330 cm^{-1} attributed to the ND lattice, confirming the formation of nanodiamond-like carbon (Ren et al., 2014), which is also evident from XRD analysis and TEM micrographs. A double-resonant 'D' band is observed at ~1365 cm^{-1}, resulting from disordered sp^2 carbon present in the sample (Ramya et al., 2016). The band centered at 1250 cm^{-1}, witnessed in the Raman spectra of fNDC, also observed in the NDs of various origin, is caused by coherence scattering of the finest fNDC grains (Mochalin et al., 2009). The band at 1450 cm^{-1} is accredited to the vibrational modes of trans-poly-acetylene (TPA) fragments present at grain boundaries (Ferrari and Robertson, 2001). Another characteristic Raman feature, commonly referred to as the 'G' band, is noticed at 1570 cm^{-1}. Several interpretations for the origin of this band, such as from sp^2 carbon clusters, mixed sp^2–sp^3 carbon, tiny graphite flakes, sp^2 chain fragments, localized interstitial C = C pairs, or other similar defects within the lattice of fNDC have been suggested (Mermoux et al., 2018). The band noticed at 1640 cm^{-1} is due to the contribution of bending vibration of OH groups from covalently attached surface functionalities and/or adsorbed water, also discerned in the fluorescence spectral analysis (Mochalin et al., 2009). In most cases, the Raman signal of a diamond is often obscured by the sp^2 carbon phases when excited by wavelengths of the visible range. This is because Raman spectroscopy is highly sensitive to the sp^2 carbon sites due to their higher polarizability and corresponding higher scattering cross-sections.

FTIR spectroscopic analysis of the synthesized fNDC was performed to study their surface states (Fig. 4). The broad band appearing between 3000 and 3700 cm^{-1} is the OH stretching peak caused by hydroxyl functional groups of alcohols, carboxyl groups, and adsorbed water covalently attached to fNDC surface. The doublet peaks observed at 2856 cm^{-1} and 2923 cm^{-1} are attributed to the C-H stretching modes of CH_2 and CH_3 groups on fNDC. The peak located at 1615 cm^{-1} is ascribed to the bending vibration of OH groups, while the shoulder peak

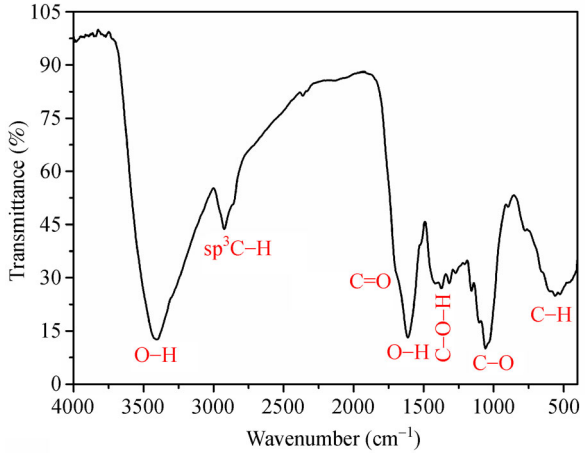

Fig. 4 FTIR transmission spectrum of the synthesized fNDC material displaying the presence of different surface functional groups.

noticed at around 1700 cm^{-1} is caused by the C = O stretching vibration of carboxylic acid (Venkatesan and Balachandran, 2020). The strong peak at 1056 cm^{-1} and its shoulder peaks at 1100 cm^{-1} and 1159 cm^{-1} could be accredited to the C-O stretching vibration of pyranose rings, epoxy, phenol, ether, and ester groups (Xiao et al., 2015b). The peak at 1269 cm^{-1} is due to the C-O bending vibration of ester. The diamond lattice vibration at 1325 cm^{-1} corresponds to the first-order Raman band of nanodiamonds. The peaks detected at 1369 cm^{-1} and 1420 cm^{-1} are ascribed to the C = O symmetric stretching of carboxyl groups. The C-H out of plane bending vibrations can be discerned between 900 and 600 cm^{-1}. The surface composition of fNDC probed by FTIR spectroscopy reveals that the synthesized fNDC are enriched with hydroxyl, carbonyl, and carboxyl functional groups with dominant hydroxyl groups, corroborating the findings of Raman and fluorescence spectral analyses.

The elemental composition of the synthesized fNDC was studied using CHNS elemental analysis, and the results, which are tabulated in Table S2, indicate that fNDC is primarily composed of carbon and oxygen. To further investigate the functional groups present in fNDC, XPS analysis was performed. The survey XPS spectrum of fNDC (refer Fig. S8) exhibits photoemissions from only C 1s and O 1s peaks, at 283.3 eV and 532.6 eV, respectively, indicating the absence of any other elements. The atomic concentrations of carbon and oxygen calculated from the area under the C 1s and O 1s peaks of the survey spectrum were 78.05% and 21.95%, respectively. Furthermore, the C 1s and O 1s regions were deconvoluted into sub-peaks to determine the content of different carbon-oxygen groups. The high-resolution C 1s XPS spectrum of fNDC was deconvoluted into seven peaks (Fig. 5(a)). The prominent peak with dominant intensity at a binding energy of 283.3 eV is attributed to the presence of the sp^3 diamond-like carbon, while the small peak at a binding energy of 284.6 eV is ascribed to the existence of sp^2 graphitic carbon (Saw and Plessis, 2004). The peaks at higher binding energies are assigned to various surface oxygen functionalities of fNDC. The broad peak at a binding energy of 285.6 eV belongs to-OH (of hydroxyl, carboxylic groups, and chemisorbed water). The peaks at 287.5 eV, 288.5 eV, and 289.7 eV correspond to C-O (of phenyl, hydroxyl, epoxy, and ester groups), C = O (of carbonyl, carboxyl, ketone, and ester groups), and COOH (of carboxylic acid), respectively. The Π- Π* satellite peak observed at a binding energy of 290.8 eV indicates the presence of delocalized Π electrons (Kumar et al., 2013).

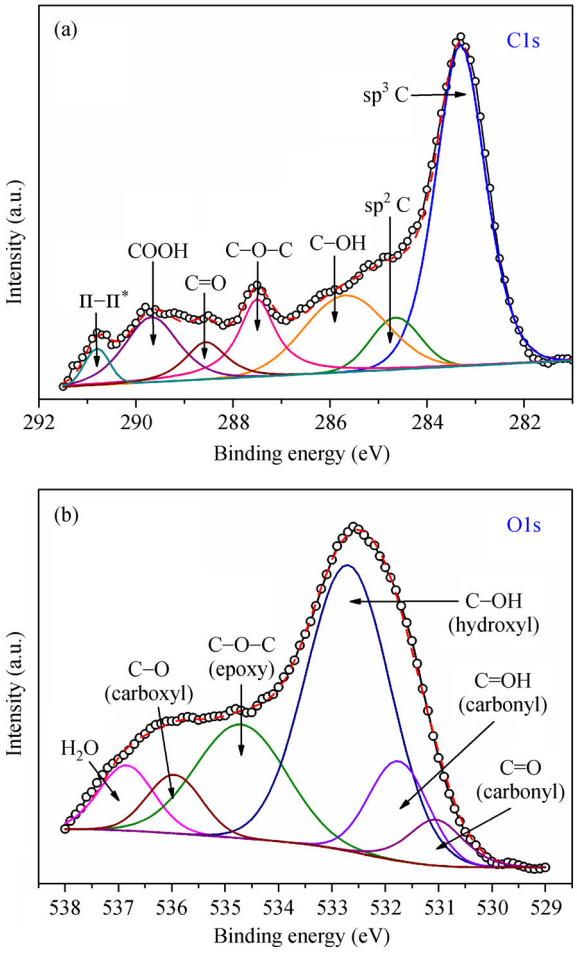

Fig. 5 High-Resolution (a) C 1s and (b) O 1s XPS spectra of fNDC fitted by Voigt line shapes after applying Shirley background. The line interconnected by circular symbols indicates the original experimental spectra, and the colored solid lines represent the deconvoluted peaks. The red dotted line represents the sum of the deconvoluted peaks.

The high-resolution O 1s XPS spectrum of fNDC, as seen in Fig. 5(b), was deconvoluted into six peaks. The peaks at binding energies of 531 eV, 531.7 eV, 532.7 eV, 534.7 eV, 536 eV, and 536.8 eV correspond to C = O (of carboxyl groups), C = O (of carbonyl groups), C-OH (of hydroxyl groups), C-O (of epoxy groups), C-O (of ether groups) and adsorbed water respectively (Fujimoto et al., 2016). Table 1 shows the atomic component fraction of

Table 1 Atomic content of C and O chemical groups in fNDC determined from C 1s and O 1s XPS spectra of fNDC

Chemical group	Chemical group content (in at %)					
C 1s	C sp^3	C sp^2	C-OH	C-O-C	C = O	COOH
	41.01	6.71	13.04	8.22	5.23	3.84
O 1s	Carboxyl C = O and C-O		C = O	C-O-C	C-OH	H_2O
	2.75		3.05	4.14	10.61	1.40

each surface functional group calculated from the area of the deconvoluted C 1s and O 1s peaks. The inspection of the relative atomic percentage of each type of oxygen group reveals that fNDC is enriched with different oxygen functional groups, dominated by hydroxyl group, as supported by FTIR, Raman, and Fluorescence spectral analyses.

The structural, elemental, morphological, and optical characterization and analyses of the synthesized sample reveal the successful valorization of agro-industrial orange peel waste to value-added fluorescent nanodiamond-like carbon material via green route. The fNDC structures exhibit remarkable optical properties and tailorable surface chemistry, making them ideal for fluorescence sensing applications.

3.4 Analytical application of the synthesized fNDC material

The interaction between fNDC and AS was studied by analyzing the fluorescence response of fNDC sensor toward AS analyte of different concentrations (Fig. 6(a)). In the absence of AS, fNDC displayed a strong fluorescence emission centered at 520 nm (λ_{exc} = 440 nm), whereas, upon the gradual addition of successive aliquots of AS, fNDC experienced fluorescence quenching. Figure 6(b) displays the Stern-Volmer plot for fluorescence quenching of fNDC by AS, exhibiting a unique dual linear relationship in the concentration ranges from 300 nM to 1 μM and from 1 μM to 10 μM. The regression equations of the relation are given by: $y_1 = 1.23 + 0.70$ C (μM) and $y_2 = 1.86 + 0.06$ C (μM), and the coefficients of determination are computed to be (R^2) are 0.9978 and 0.9984 respectively, fitted from the least-squares method. The limit of detection (LOD) of the two regression equations is estimated to be as low as 34.42 nM and 356.46 nM, respectively. The linear response of the Stern-Volmer model of AS-induced fluorescence quenching of fNDC reveals a dynamic quenching mechanism, indicating that either resonance energy transfer or electron transfer has occurred between AS and fNDC (Yen et al., 2019). The resonance energy transfer mechanism can be ruled out because AS has no absorption above 300 nm wavelength, and hence its absorption spectrum does not overlap with the emission spectrum of fNDC (refer Fig. S9) (Pallikkarathodi Mani et al., 2018). To investigate the possibility of an electron transfer mechanism between fNDC and AS, cyclic voltammetry (CV) measurements were performed to determine their HOMO and LUMO energy levels. From the CV data (refer Fig. S10 and Table S3 for details), the HOMO and LUMO energy levels of fNDC and AS were calculated to be −6.63, −1.22, −6.86 and −2.74, respectively. As the LUMO level of AS is lower than that of fNDC, electron transfer from fNDC to AS could occur, supporting fluorescence quenching via electron transfer.

To study the influence of pH on the fluorescence response of the synthesized fNDC in the presence and absence of AS, the fluorescence emission intensity of fNDC was monitored in the pH range between 2 and 12 (Fig. S11). It is noticed that the fluorescence intensity of fNDC witnessed a slight decrease at pH below 4 and above 9 due to the ionization of the surface functional groups of fNDC, which in turn affected its fluorescence intensity. The quenching of fluorescence of fNDC on the addition of AS (5 μM) was observed over the entire pH range with slight variations in the pH below 4 and above 9, in the acidic and alkaline environments, respectively.

To assess the validity and test the selectivity of fNDC sensor, fluorescence measurements were performed in the presence of a fixed concentration (10 μM) of various interfering species, namely scopolamine, glucose, ascorbic acid, uric acid, K^+, Na^+, Ca^{2+}, Mg^{2+}, Fe^{3+}, and Cu^{2+} prepared under identical experimental conditions. The

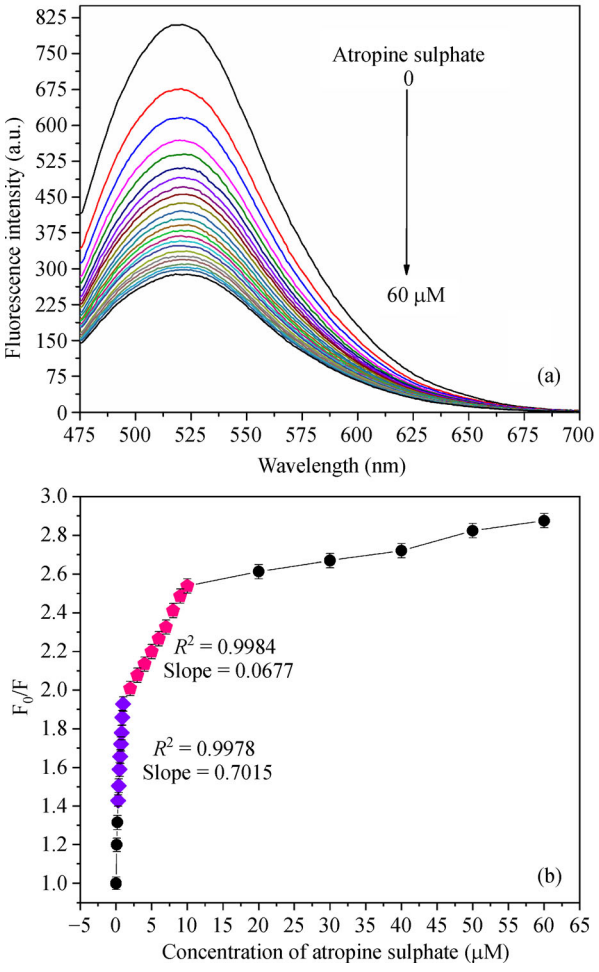

Fig. 6 (a) Fluorescence emission spectra of 25 μg/mL fNDC (λ_{exc} = 440 nm and λ_{em} = 520 nm) for increasing concentrations of AS in PBS (pH = 7). (b) The relative intensity (F_0/F) plot of fluorescence quenching of fNDC for varying concentrations of AS, exhibiting dynamic linear range (F_0 and F, represent the fluorescence intensity of fNDC in the absence and presence of AS).

Table 2 Analytical performance of fNDC sensor for various concentrations of AS in biological fluids and pharmaceutical formulations

Sample	Atropine sulfate (μM)		Recovery (%)	*RSD (%) (n = 3)
	Spiked	Found		
Human Blood Serum	0.30	0.28	96.06	0.39
	0.60	0.62	103.01	0.36
	0.90	0.88	97.78	0.29
Human Urine	0.30	0.32	103.68	0.39
	0.60	0.59	97.33	0.30
	0.90	0.89	98.49	0.25
Atropine sulfate 1 mL ampoules (0.6 mg/mL)	0.30	0.29	97.83	0.33
	0.60	0.62	102.18	0.39
	0.90	0.88	97.33	0.28
Atropine 1% 5 mL eye drop (10 mg/mL)	0.30	0.31	103.45	0.38
	0.60	0.58	98.68	0.31
	0.90	0.91	101.56	0.35

selectivity of the sensor was evaluated by plotting the fluorescence intensity ratios of fNDC against the interfering species. As seen in Fig. 7, AS showed a remarkable quenching effect on the fluorescence emission intensity of fNDC, whereas no quenching/ negligible quenching was noticed in the presence of other interfering species. The relative error of the interference effect of common interferents was below 3%, which is within the tolerable limit. These observations apparently confirm that the developed fNDC sensor is highly selective toward the detection of AS.

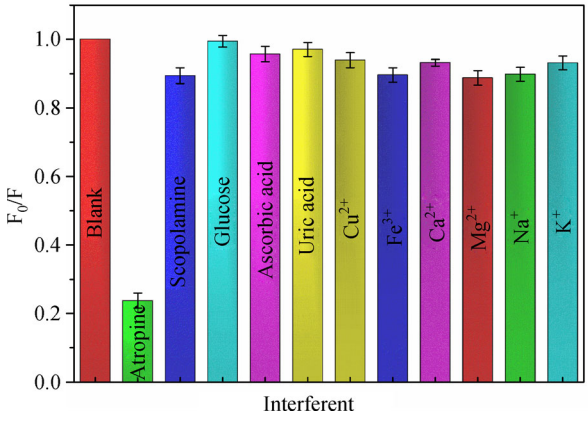

Fig. 7 Fluorescence intensity ratio response of fNDC to AS and other potential interferents in PBS (λ_{exc} = 440 nm and λ_{em} = 525 nm; interferents = 10 μM; fNDC = 25 μg/mL; pH = 7).

Having established that fNDC sensor can effectively detect AS, it is equally essential to determine the versatility of this sensor for applications in a multidisciplinary arena. Hence, the applicability of fNDC sensor was validated by detecting AS spiked in biological samples (human serum and urine) and pharmaceuticals (AS injection and eye drop), using the standard addition method. Briefly, three different concentrations of AS were spiked in human serum and urine, and three different concentrations of AS injection and eye drop were prepared. The fluorescence spectra were recorded at an excitation wavelength of 440 nm, and emission intensity was monitored at 520 nm wavelength. From the data collected from triplicate experiments, the concentrations of spiked samples were calculated from the plots (Fig. S12 (a–d)), and the values are tabulated in Table 2. The recovery rates of AS ranged from 96% to 104%, with Relative Standard Deviations (RSDs) of less than 0.4%, indicating the accuracy of the fabricated sensor.

Table S4 displays the analytical figures of performance for the quantification of AS by various sensors in previous studies as well as the current study. In comparison to the other reported sensors for the detection of AS, fNDC sensor has advantages in several aspects. Unlike other sensors that require expensive and/or complex and time-consuming synthesis and fabrication techniques, fNDC sensor was created by valorizing agro-industrial fruit peel waste through a cost-effective and simple green route. The fNDC sensor is highly versatile, with excellent reproducibility, high stability, exceptional sensitivity, and anti-interference ability. It exhibits an ultralow detection limit for determining AS in body fluids and pharmaceuticals.

4 Conclusions

A novel fNDC sensor was successfully developed by valorizing agro-industrial orange peel waste via a cost-effective, hassle-free, scalable, and facile green route. The fNDC sensor was employed for highly sensitive and

selective fluorescence detection of the hazardous tropane alkaloid AS. The sensor demonstrated broad and unique dual linearity over concentration ranges of 300 nM to 1 μM and 1 μM to 10 μM, with superior ultralow sensitivity of 34.42 nM and 356.46 nM, respectively. Furthermore, the sensor was shown to be an excellent fluorescent probe for the detection of AS in biological fluids and pharmaceutical formulations. According to our findings, fNDC sensor is a highly reliable fluorescent probe for the precise quantification of the life-threatening alkaloid AS in real samples. The sensor portrays significant potential for use in clinical pharmacokinetics, pharmaco-toxicology, quality control, and forensics.

Pantent and Data availability This work is a part of a patent application filed with the Indian Patent Office.(Details: A. V. Ramya and Manoj. B, CHRIST (Deemed to be University), Indian Patent App. Number: 202041033633, published on 21st August 2020.). The data sets generated during and/or analyzed during the current study shall be available from the corresponding author on reasonable request.

Acknowledgements The authors would like to thank the Centre for Research, CHRIST (Deemed to be University), Bengaluru, for facilitating this work. AVR is thankful to DST - INSPIRE for the fellowship Grant (DST/INSPIRE/03/2015/004970). We also acknowledge CeNSE IISc, Bengaluru, IUCNN MG University, Kottayam and SAIF, CUSAT, Cochin for the characterization facilities.

Electronic Supplementary Material Supplementary material is available in the online version of this article at https://doi.org/10.1007/s11783-021-1461-z and is accessible for authorized users.

References

Bray K, Previdi R, Gibson B C, Shimoni O, Aharonovich I (2015). Enhanced photoluminescence from single nitrogen-vacancy defects in nanodiamonds coated with phenol-ionic complexes. Nanoscale, 7 (11): 4869–4874

Dar R A, Brahman P K, Tiwari S, Pitre K S (2012). Electrochemical determination of atropine at multi-wall carbon nanotube electrode based on the enhancement effect of sodium dodecyl benzene sulfonate. Colloids and Surfaces. B, Biointerfaces, 91(1): 10–17

Ferrari A C, Robertson J (2001). Origin of the 1150 cm^{-1} Raman mode in nanocrystalline diamond. Physical Review B: Condensed Matter and Materials Physics, 63(12): 2–5

Fujimoto A, Yamada Y, Koinuma M, Sato S (2016). Origins of sp^3C peaks in C1s X-ray photoelectron spectra of carbon materials. Analytical Chemistry, 88(12): 6110–6114

Hao J, Pan L, Gao S, Fan H, Gao B (2019). Production of fluorescent nano-diamonds through femtosecond pulsed laser ablation. Optical Materials Express, 9(12): 4734-4741

Hsiao W, Hui Y Y, Tsai P C, Chang H C (2016). Fluorescent nanodiamond: A versatile tool for long-term cell tracking, super-resolution imaging, and nanoscale temperature sensing. Accounts of Chemical Research, 49(3): 400–407

Jariwala D H, Patel D, Wairkar S (2020). Surface functionalization of nanodiamonds for biomedical applications. Materials Science and Engineering C, 113: 110996

Kerchner A, Farkas Á (2020). Worldwide poisoning potential of *Brugmansia* and *Datura*. Forensic Toxicology, 38(1): 30–41

Khataee A, Hassanzadeh J, Kohan E (2018). Specific quantification of atropine using molecularly imprinted polymer on graphene quantum dots. Spectrochimica Acta. Part A: Molecular and Biomolecular Spectroscopy, 205: 614–621

Kumar A, Ann Lin P, Xue A, Hao B, Khin Yap Y, Sankaran R M (2013). Formation of nanodiamonds at near-ambient conditions via microplasma dissociation of ethanol vapour. Nature Communications, 4(1): 1–9

Kumar R, Pandit P, Pal P, Dhakate S R, Pant R P, Kumar R, Avasthi D K, Singh D K (2018). Engineering bright fluorescent nitrogen-vacancy (NV) nano-diamonds: Role of low-energy ion-irradiation parameters. AIP Advances, 8(8): 085023

Kurbatov A V, Mayewski P A, Steffensen J P, West A, Kennett D J, Kennett J P, Bunch T E, Handley M, Introne D S, Que Hee S S, Mercer C, Sellers M, Shen F, Sneed S B, Weaver J C, Wittke J H, Stafford T W, Donovan J J, Xie S, Razink J J, Stich A, Kinzie C R, Wolbach W S (2010). Discovery of a nanodiamond-rich layer in the Greenland ice sheet. Journal of Glaciology, 56(199): 747–757

Lai S, Jin Y, Shi L, Zhou R, Zhou Y, An D (2020). Mechanisms behind excitation- and concentration-dependent multicolor photoluminescence in graphene quantum dots. Nanoscale, 12(2): 591–601

Mandal M, Haso F, Liu T, Fei Y, Landskron K (2014). Size tunable synthesis of solution processable diamond nanocrystals. Chemical Communications, 50(77): 11307–11310

Pallikkarathodi Mani N, Ganiga M, Cyriac J (2018). MoS_2 nanohybrid as a fluorescence sensor for highly selective detection of dopamine. Analyst (London), 143(7): 1691–1698

Meneguzzo F, Brunetti C, Fidalgo A, Ciriminna R, Delisi R, Albanese L, Zabini F, Gori A, dos Santos Nascimento L, De Carlo A, Ferrini F, Ilharco L, Pagliaro M (2019). Real-scale integral valorization of waste orange peel via hydrodynamic cavitation. Processes (Basel, Switzerland), 7(9): 581

Mermoux M, Chang S, Girard H A, Arnault J C (2018). Raman spectroscopy study of detonation nanodiamond. Diamond and Related Materials, 87: 248–260

Mochalin V N, Shenderova O, Ho D, Gogotsi Y (2012). The properties and applications of nanodiamonds. Nature Nanotechnology, 7(1): 11–23

Mochalin V, Osswald S, Gogotsi Y (2009). Contribution of functional groups to the Raman spectrum of nanodiamond powders. Chemistry of Materials, 21(2): 273–279

Nunn N, Torelli M, McGuire G, Shenderova O (2017). Nanodiamond: A high impact nanomaterial. Current Opinion in Solid State and Materials Science, 21(1): 1–9

Ramya A V, Mohan A N, Manoj B (2016). Wrinkled graphene: Synthesis and characterization of few layer graphene-like nanocarbons from kerosene. Materials Science Poland, 34(2): 330–336

Ren X D, Yang H M, Zheng L M, Yuan S Q, Tang S X, Ren N F, Xu S D (2014). A conversion model of graphite to ultrananocrystalline diamond via laser processing at ambient temperature and normal pressure. Applied Physics Letters, 105(2): 021908

Saw K G, du Plessis J (2004). The X-ray photoelectron spectroscopy C 1s diamond peak of chemical vapour deposition diamond from a sharp interfacial structure. Materials Letters, 58(7–8): 1344–1348

Shenderova O, Nunn N, Oeckinghaus T, Torelli M, McGuire G, Smith K, Danilov E, Reuter R, Wrachtrup J, Shames A, Filonova D, Kinev A (2017). Commercial quantities of ultrasmall fluorescent nanodiamonds containing color centers. In: Advances in Photonics of Quantum Computing, Memory, and Communication. International Society for Optics and Photonics, 1011803

Stursa J, Havlik J, Petrakova V, Gulka M, Ralis J, Zach V, Pulec Z, Stepan V, Zargaleh S A, Ledvina M, Nesladek M, Treussart F, Cigler P (2016). Mass production of fluorescent nanodiamonds with a narrow emission intensity distribution. Carbon, 96: 812–818

Sun D, Ban R, Zhang P H, Wu G H, Zhang J R, Zhu J J (2013). Hair fiber as a precursor for synthesizing of sulfur- and nitrogen-co-doped carbon dots with tunable luminescence properties. Carbon, 64: 424–434

Tang H, Wang M, He D, Zou Q, Ke Y, Zhao Y (2016). Synthesis of nano-polycrystalline diamond in proximity to industrial conditions. Carbon, 108: 1–6

Tom N R, Varghese G H, Alexander H, Swethalekshmi V, Kumar T R, Sivakumar T (2016). A case report on atropine induced psychosis. International Journal of Pharmaceutical Sciences and Research, 7(1): 387–391

Venkatesan R A, Balachandran M (2020). Novel carbon nano-onions from paraffinum liquidum for rapid and efficient removal of industrial dye from wastewater. Environmental Science and Pollution Research International, 27(35): 43845–43864

Wikandari R, Nguyen H, Millati R, Niklasson C, Taherzadeh M J (2015). Improvement of biogas production from orange peel waste by leaching of limonene. BioMed Research International, 2015: 1–6

Xiao J, Liu P, Li L, Yang G W (2015). Fluorescence origin of nanodiamonds. Journal of Physical Chemistry C, 119(4): 2239–2248

Xiao J, Liu P, Yang G W (2015). Nanodiamonds from coal under ambient conditions. Nanoscale, 7(14): 6114–6125

Yen Y T, Lin Y S, Chen T Y, Chyueh S C, Chang H T (2019). Carbon dots functionalized papers for high-throughput sensing of 4-chloroethcathinone and its analogues in crime sites. Royal Society Open Science, 6(9): 191017

Zhang W, Niu X, Chen X, Guo X, Wang J, Fan J (2016). Universal role of oxygen in full-visible-region photoluminescence of diamond nanocrystals. Carbon, 109: 40–48